*Geophys. J. Int.* (1998) **134**, 243–253

# Improved ocean-geoid resolution from retracked ERS-1 satellite altimeter waveforms

Stefan Maus,[1,*] Chris M. Green[2] and J. Derek Fairhead[2]

[1] *Department of Earth Sciences, University of Leeds, Leeds* LS2 9JT, *UK*
[2] *GETECH, Department of Earth Sciences, University of Leeds, Leeds* LS2 9JT, *UK*

Accepted 1998 February 3. Received 1998 January 8; in original form 1997 June 30

## SUMMARY

The ocean geoid can be inferred from the topography of the mean sea surface. Satellite altimeters transmit radar pulses and determine the return traveltime to measure sea-surface height. The ERS-1 altimeter stacks 51 consecutive radar reflections on board the satellite to a single waveform. Tracking the time shift of the waveform gives an estimate of the distance to the sea surface. We retrack the ERS-1 radar traveltimes using a model that is focused on the leading edge of the waveforms. While earlier methods regarded adjacent waveforms as independent statistical events, we invert a whole sequence of waveforms simultaneously for a spline geoid solution. Smoothness is controlled by spectral constraints on the spline coefficients. Our geoid solutions have an average spectral density equal to the expected power spectrum of the true geoid. The coherence of repeat track solutions indicates a spatial resolution of 31 km, as compared to 41 km resolution for the ERS-1 Ocean Product. While the resolution of the latter deteriorates to 47 km for wave heights above 2 m, our geoid solution maintains its resolution of 31 km for rough sea. Retracking altimeter waveform data and constraining the solution by a spectral model leads to a realistic geoid solution with significantly improved along-track resolution.

**Key words:** fractals, geodesy, geoid anomalies, gravity, Satellite Geodesy, waveform analysis.

## 1 INTRODUCTION

Since publication of the first satellite gravity maps (Haxby *et al.* 1983; Rapp 1983), spatial wavelength resolution of satellite gravity has improved considerably, primarily due to the denser track spacing of 6 km and 8 km at the equator during the geodetic missions of Geosat (1985–1990) and ERS-1 (1991–1996), respectively. Satellite gravity is computed by geodetic Fourier methods (Schwarz, Sideris & Forsberg 1990) from gridded geoid profiles (Haxby *et al.* 1983) or vertical deflection of the geoid (Sandwell & McAdoo 1990). See Olgiati *et al.* (1995) for a comparison of the two methods. A detailed description of marine gravity mapping from satellite altimetry is given by Sandwell & Smith (1997). Satellite altimeters measure mean sea-surface height, which is controlled primarily by the Earth's gravity field, but is also subject to tides, ocean currents and atmospheric effects. In satellite gravity these secondary effects are regarded as noise. After applying various corrections, the sea-surface heights serve as estimates of the ocean geoid.

Resolution of along-track geoid profiles can be defined as the wavelength at which the mean square coherence between two exact repeat tracks falls to below 0.5 (Marks & Sailor 1986). With this definition along-track geoid resolution has improved from 110 km for 1975–1978 Geos-3 data to 50 km for 1978 Seasat data (Marks & Sailor 1986). In a detailed study of along-track geoid resolution, Yale, Sandwell & Smith (1995) find a global average resolution of 38 km and 43 km for pre-edited Geosat and ERS-1 data, respectively. Along-track resolution can be improved to below 30 km by stacking corrresponding tracks of the exact repeat missions (ERM), called a multidisciplinary phase for ERS-1. However, the ERM have a track spacing of 164 km (Geosat) and 80 km (ERS-1), which is too wide for high-resolution gravity mapping. During the geodetic missions, on the other hand, tracks are not repeated and it is essential to extract as accurate geoid information as possible from every recorded track. This can be achieved by reprocessing the raw radar waveform data.

After outlining the basic principles of satellite radar altimetry, we propose a simplified waveform model to improve tracking. Instead of tracking individual traveltimes, we process a whole

* Now at: Institut für Geophysik und Meteorologie der Technischen Universität Braunschweig, Mendelssohnstr. 3, 38106 Braunschweig, Germany. E-mail:smaus@gwdg.de.

sequence of waveforms simultaneously, using a polynomial spline to represent the geoid. To separate geoid signal from noise, one requires a spectral model for the true geoid. Using a relationship between geoid and gravity, we infer the geoid spectrum from large-scale land and marine gravity grids. The expected spectrum of the true geoid is then utilized to constrain the smoothness of the spline geoid solutions, thus suppressing noise at the tracking stage. We tested the algorithm on three repeat cycles of the ERS-1 ERM. Coherencies indicate a significant improvement in along-track resolution, in particular for rough sea states.

## 2 BASIC PRINCIPLES

After correcting for tides and currents, as far as possible, sea-surface height provides an estimate of the ocean geoid $N$ which is related to the gravity potential $V$ by Brun's approximate formula:

$$V(x, y, 0) = g_0 N(x, y), \quad (1)$$

where $g_0$ is the gravity constant. Satellite altimeters are able to measure the sea-surface height by sending down radar pulses that are reflected at the sea surface and recorded back at the satellite. Since the satellite's smooth orbital path and position are known accurately at any instant, the sea-surface topography relative to a reference ellipsoid can be determined. The distance between satellite and sea surface is referred to as the range. The range must be measured to an accuracy of centimetres in order to derive geoid anomalies down to wavelengths of 20 km and less.

The energy of the radar pulse reflected from the sea surface does not return to the satellite as a sharp pulse, but is scattered over a considerable period of time. The power of the return signal as a function of time is called a waveform. The waveforms are sampled in 3.03 ns intervals (gates) corresponding to 45 cm in range. Examples of waveforms resulting from calm and rough seas are displayed in Fig. 1. This figure shows the change in the waveform shape from impulsive to emergent. The ERS-1 satellite transmits 1020 radar pulses per second. Some 51 consecutive returns are averaged on board the satellite and transmitted to the receiver stations as 20 average waveforms per second, or one every 330 m along-track. On reaching the sea surface, the radar pulse has an effective geodetic footprint between 2 and 7 km, depending on the sea state. Energy reflected at the centre of the footprint returns to the satellite earlier than energy reflected at the edges of the footprint. The power of the returning pulse therefore increases from zero to some maximum value over a time interval of about 6–60 ns. This period is referred to as the leading edge. The traveltime is the time to the centre of the leading edge. The steeper the leading edge, the more accurately the centre time of the leading edge can be estimated. The slope of the leading edge depends not only on the diameter of the footprint but also on the roughness of the sea. The calmer the sea, the steeper the leading edge. The subsequent decrease in power is referred to as the trailing edge. The slope of the trailing edge is correlated with the surface wind speed.

## 3 STANDARD WAVEFORM ANALYSIS

ERS-1 satellite altimeter products currently used by the Geoscience community are derived from on-board estimates of the return traveltime. The ERS-1 on-board tracker uses a model of the return waveform of Brown (1977). Apparently, it was considered to reprocess the waveforms later (Tokmakian *et al.* 1994) using an algorithm of Challenor & Strokosz (1989). The on-board tracking algorithm is based on a waveform model accounting for three waveform parameters: the return traveltime, the significant wave height, and the backscattered power (related to the surface wind speed). Each waveform is

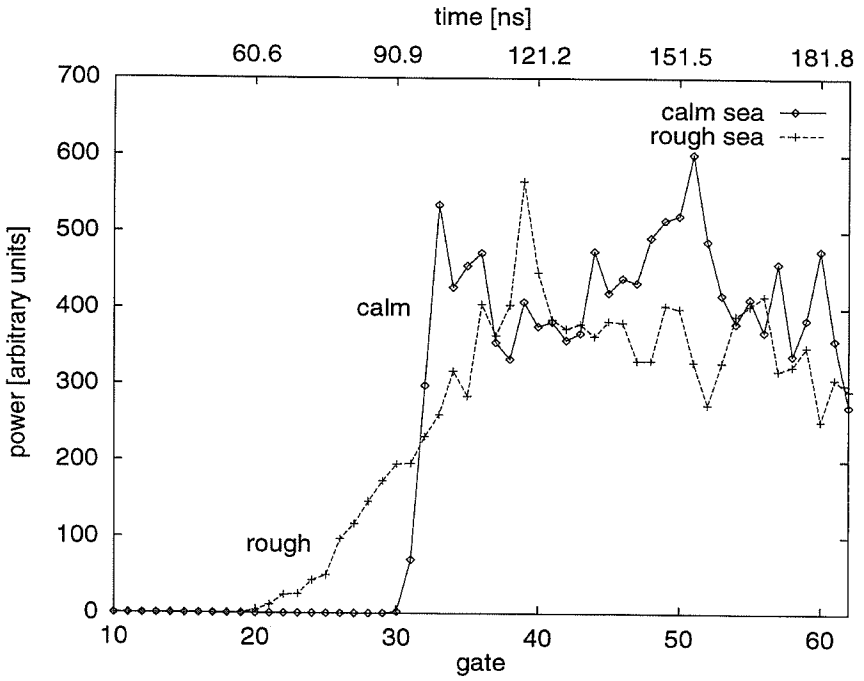


**Figure 1.** Examples of ERS-1 return radar waveforms for calm (wave height less than 1 m) and rough seas (mean wave height 11 m). The two waveforms differ in the slope of the leading edge as well as in overall amplitude.

analysed separately. The 20 Hz traveltime estimates are combined to 10 Hz semi-elementary and 1 Hz averages. After applying tidal and atmospheric corrections, these are the ERS-1 Ocean Product (OPR) geoid solutions incorporated in current satellite gravity maps.

## 4 IMPROVED TRAVELTIME ESTIMATES FROM RETRACKING

For the purpose of estimating geoid height, the only waveform parameter of interest is the return traveltime. Traveltime estimates can be optimized by concentrating on the exact location of the leading edge. Without attempting to explain the full shape of the waveforms, we re-align the waveforms using a simplified waveform model $M$ with

$$M(\text{amp}, \sigma, \tau; t) = \frac{\text{amp}}{2}\{1 + \text{erf}[\sigma(t - 31 + \tau)]\}, \qquad (2)$$

where amp is the amplitude of the waveform, $\sigma$ controls the slope of the leading edge, $\tau$ is the centre time (lag) of the leading edge, $t$ is the time along the waveform and erf is the error function. Both $\tau$ and $t$ are measured in gates, and can be non-integer values. An example of this model curve is shown as a dashed line in Fig. 2.

To find the optimum centre positions $\tau_k$ of a sequence of $nw$ waveforms $W_k(t)$, with $k = 1 \ldots nw$, we use an $L_2$-norm misfit function $E$ with

$$E(\text{amp}, \sigma, \tau_1, \ldots, \tau_{nw}) = \sum_{k=1}^{nw} \sum_{i=\text{mingate}}^{\text{maxgate}} \left[\frac{W_k(i) - M(\text{amp}, \sigma, \tau_k; i)}{W_k(i) + \text{offset}}\right]^2. \qquad (3)$$

The smaller the chosen value of offset, the more significance is placed on the lower front of the leading edge. With amplitudes around 400, a value of offset = 50 produces good results. Mingate and maxgate have to be chosen in such a way as to include precisely the full leading edge, taking into account its varying centre position and slope.

We find the minimum of the misfit function in eq. (3) by a modified Gauss–Newton algorithm, using the analytical first and second derivatives of $E(\text{amp}, \sigma, \tau_1, \ldots, \tau_{nw})$. We rescale the parameters amp and $\sigma$ by $\sigma' = \ln \sigma$ and $\text{amp}' = (\text{amp} + \text{amp}_{\text{offset}})/\text{amp}_{\text{factor}}$ so that amp′ and $\sigma'$ have an expected value of zero at the solution and a unit perturbation leads to an equal change in the misfit function for all parameters. The optimization for a sequence of $nw$ waveforms yields return traveltime corrections $\tau_1 \ldots \tau_{nw}$ which are added onto the OPR return traveltimes. The improvement in the corresponding ranges is demonstrated in Fig. 2, which shows a sequence of consecutive waveforms, normalized on the OPR estimate of the waveform onset. The retracked waveforms show a significant decrease in scatter.

Fig. 3 shows the improved quality of retracked geoid height estimates. Nevertheless, retracking alone does not completely remove the high-frequency noise. This noise is due to the uncertainty of tracking waveforms which are sampled at a bin width of 3.03 ns, corresponding to 45.45 cm in range. To reduce this high-frequency noise, the practice until now has been to compute 1 s averages of the 1/20 s range estimates. However, the resulting 1 Hz ranges (e.g. Fig. 4) are still noisy and have to undergo further low-pass filtering before they can be used in subsequent processing stages. The OPR also provides 10 Hz

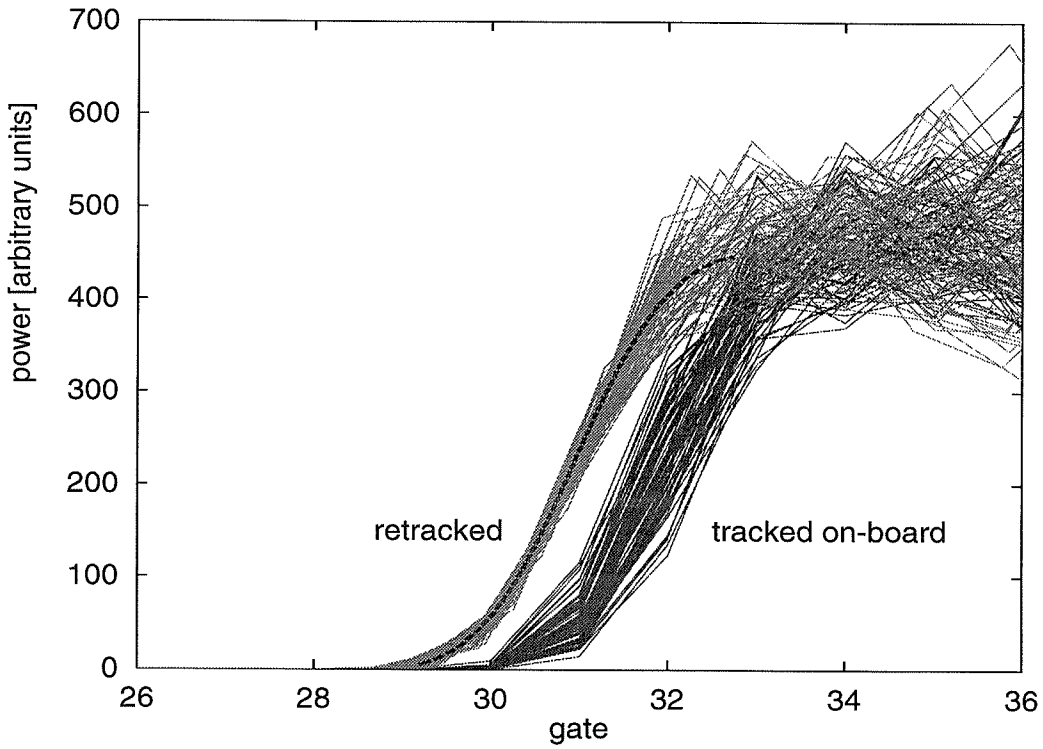


**Figure 2.** Tracking is equivalent to locating the centre position of the leading edge. The performance of a tracking algorithm can be verified by aligning the waveforms in such a way that the estimated centre of the leading edge is at a fixed gate (here gate 32 for OPR and gate 31 for this study's retracks). The superior quality of the retracked traveltimes leads to a significantly reduced variance of the waveforms at the leading edge. Here, 80 consecutive waveforms (4 s of data) are displayed. The model of eq. 2 is indicated as a dashed line.

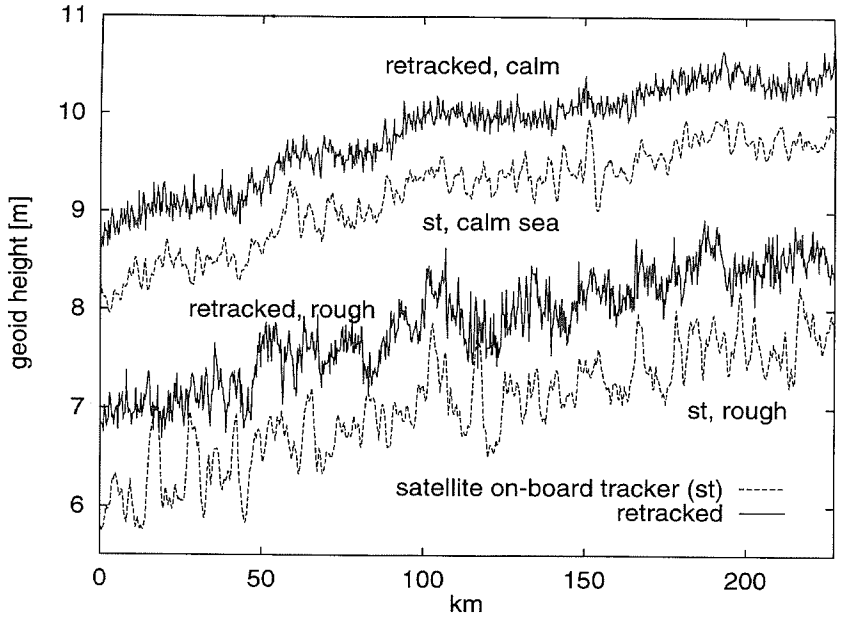


**Figure 3.** Satellite on-board tracker (st) versus retracked geoid heights for two repeat tracks with calm and very rough sea conditions from a low-signal–high-noise area (45°S, 130°E) in the southern Pacific Ocean. Retracking significantly reduces the noise at intermediate wavelengths. This is particularly obvious for the calm sea track. Offsets have been added to separate the signals for clarity.

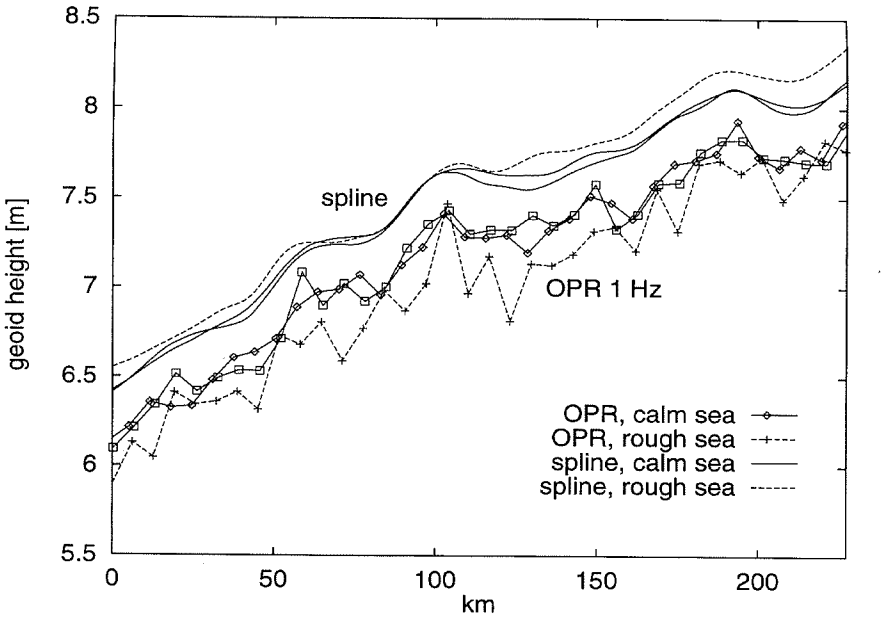


**Figure 4.** OPR 1 Hz geoid heights versus this study's spline geoid solutions for three repeat tracks. Offsets have been added to separate the two kinds of solutions for clarity. Our constrained spline geoid solution shows a remarkable degree of consistency in the repeat profiles, even for the track with very rough sea (mean wave height $>10$ m).

semi-elementary averages, which are sometimes used instead of the 1 Hz averages.

Instead of filtering the 20 Hz range estimates, we suppress noise at the tracking stage. This is achieved by using splines to model the geoid and by imposing smoothness constraints on the polynomial coefficients of the spline.

## 5 SPLINE GEOID SOLUTION

Instead of estimating traveltimes from individual waveforms, we invert a 20 s sequence (132 km window) of 408 waveforms simultaneously. The $k$th radar pulse (actually 51 pulses) was reflected from the sea surface at $utc_k$ universal time. The time stamp $utc_k$ can be translated to the exact location of the satellite. Let $y_k$ be the corresponding (unknown) true geoid height. $y_k$ can then be expressed as a geoid polynomial with respect to universal time $utc_k$ as

$$y_k = \sum_{j=0}^{n} a_j T_j(utc_k), \tag{4}$$

where $T_j$ are the base polynomials of order $j$, $n$ is the maximum order and $a_j$ are the coefficients of the polynomial. We

utilize powers of cosine as base polynomials, up to an order of $n = 40$. With a window size of 132 km we are thus able to represent wavelengths down to 6 km, corresponding to the approximate across-track resolution of combined Geosat and ERS-1 data. The 6 km cut-off is clearly visible in the spline spectrum of Fig. 5.

The geoid height $y_k$ to be estimated is related to the OPR range $z_k$ by

$$y_k = \mathrm{alt}_k - z_k + (3.03\ \mathrm{ns} \cdot c \cdot \tau_k)/2, \tag{5}$$

where $\mathrm{alt}_k$ is the altitude of the satellite above the reference ellipsoid, $c$ is the speed of light and $\tau_k$ is the lag correction of the $k$th waveform, measured in gates of 3.03 ns. This gives an expression

$$\tau_k(a_0, \ldots, a_n) = \frac{2}{3.03\ \mathrm{ns}\ c}\left[z_k - \mathrm{alt}_k + \sum_{j=0}^{n} a_j T_j(utc_k)\right] \tag{6}$$

relating the lag corrections of the waveforms to the coefficients of the geoid polynomial of eq. (4). In the previous section, eqs (2) and (3) were utilized to compute lag corrections for the OPR return traveltimes. Substituting $\tau_k(a_0, \ldots, a_n)$ of eq. (6) for $\tau$ in eq. (2) and using the same misfit function of eq. (3), we can now optimize 41 geoid polynomial coefficients $a_j$ instead of 408 individual waveform lags $\tau_k$. The optimum lags $\tau_k$ can then be computed from the optimum coefficients $a_0, \ldots, a_n$ using eq. (6). For the optimization, the coefficients again have to be rescaled in order to have an expected value of zero near the solution, which is achieved by a simple linear transform. For 408 waveforms and a polynomial of degree 40, the modified Gauss–Newton algorithm converges within five to eight iterations. Solutions in adjacent windows are combined to a spline geoid solution.

One of the advantages of this approach is that spectral constraints can be imposed in the optimization on the coefficients of the spline. If no constraints are imposed, the geoid solution is smooth but tends to oscillate (Fig. 6). The corresponding power spectrum of the along-track geoid (Fig. 5) has the typical curved shape of gravity power spectra at long wavelengths (see Fig. 7 and the discussion in the following section), but turns white (=noisy) towards short wavelengths. For a realistic geoid the spectrum should continue decreasing with a slope that can be determined from non-satellite gravity grids as follows.

## 6 EXPECTED POWER SPECTRUM OF THE TRUE GEOID

A spectral model for the geoid can be inferred from the power spectra of free-air gravity data. Let us assume that the statistical properties of free-air gravity over land (for which large, accurate grids are readily available) are comparable to those of ocean gravity. Fig. 7 shows the free-air and Bouguer gravity power spectra of a $4000 \times 4000\ \mathrm{km}^2$ area of the Siberian craton in log–log scale. Starting at short wavelengths (right), both power spectra increase towards long wavelengths (left) with a steady slope of 4.5, indicating self-similarity of the gravity field with a scaling exponent of $\lambda_g^{2D} = 4.5$. Here the index 2D indicates that this is the scaling exponent of the 2-D power spectrum, which is different from the 1-D power spectrum of profiles of the same data set (Maus & Dimri 1994). The scaling exponent governs the overall smoothness of a random function. High values indicate a smooth function, whereas low values indicate roughness. White noise has a scaling exponent of zero.

It is interesting to note that at short wavelengths free-air and Bouguer gravity follow the same scaling law, reflected in equal scaling exponents. The self-similarity of the gravity field is probably due to a self-similar density distribution in the crust (Pilkington & Todoeschuck 1990; Maus & Dimri 1996) combined with self-similar topographic anomalies (Chapin

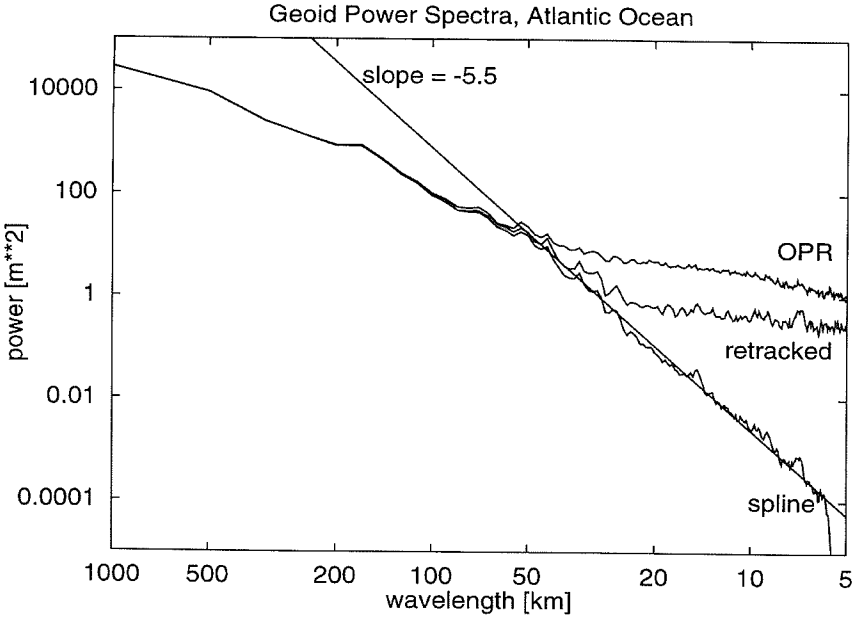


**Figure 5.** Power spectra of along-track geoid solutions estimated using a 1140 km window. The line with a slope of −5.5 depicts the expected power spectrum of the true geoid at short wavelengths. Noise begins to dominate the OPR geoid at wavelengths around 50 km. As reflected in these power spectra, this noise can be reduced significantly by retracking the waveforms. A truly realistic geoid solution can be obtained by using a polynomial spline and imposing spectral constraints on the polynomial coefficients in the inversion.

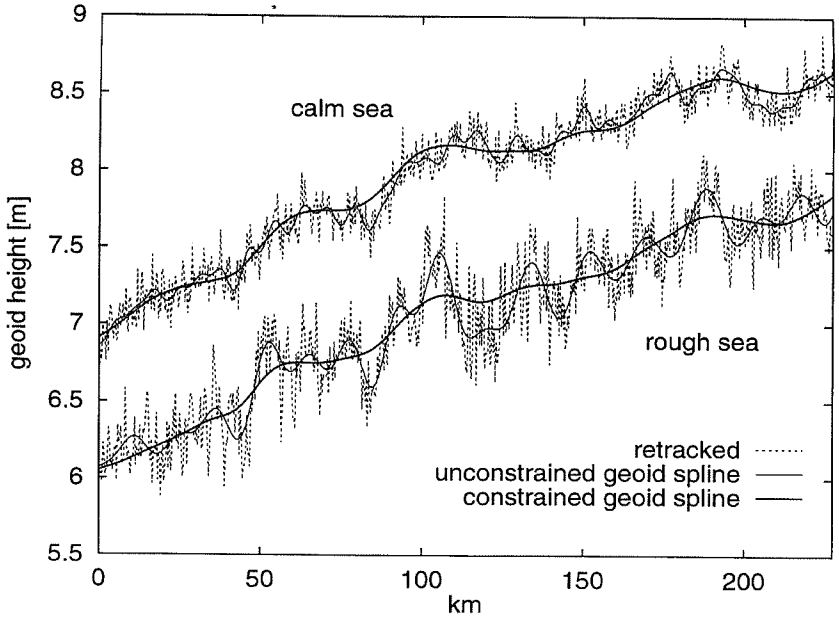


**Figure 6.** Spline geoid solutions superimposed on the retracked geoid height estimates for two repeat tracks. Offsets have been added to separate the two tracks for clarity. Fitting an unconstrained polynomial directly to the retracked heights leads to unwanted oscillations in the geoid solution. These oscillations can be removed by imposing a penalty for high power in high-order polynomial coefficients and fitting the thus constrained polynomial directly to the waveform data. It is important to understand that the polynomial is not fitted to the retracked traveltimes. Instead, the original waveforms are processed using a polynomial as a continuous geoid model. Thus, we estimate 41 geoid polynomial coefficients instead of 408 individual traveltimes in each window. Polynomials in overlapping windows are combined to a spline geoid solution.

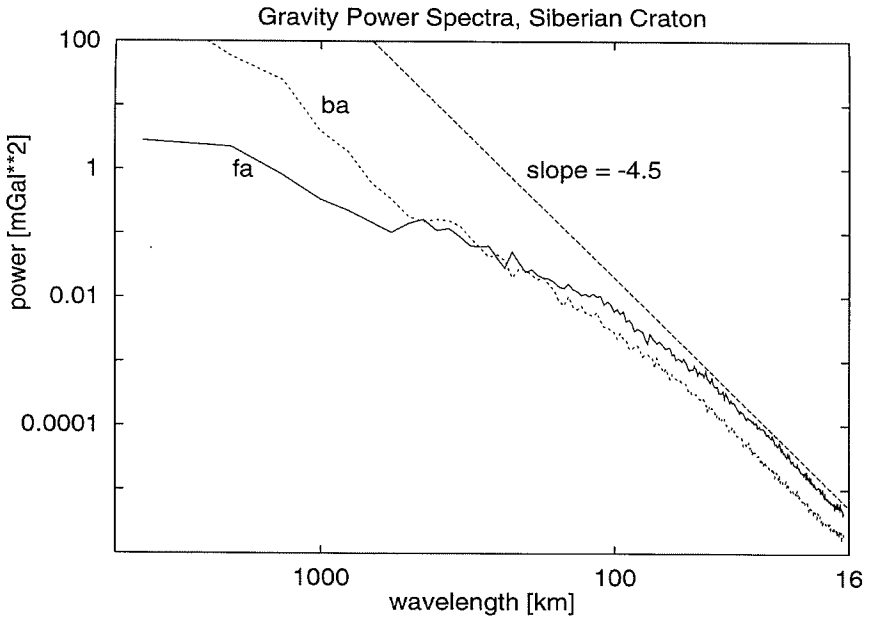


**Figure 7.** Sample power spectra for 8 km free-air (fa) and Bouguer anomaly (ba) grids of a $4000 \times 4000\ km^2$ area covering the Siberian craton. Grids in Lambert Conformal projection. Due to the absence of topographic anomalies, Bouguer has less power at short wavelengths than free-air gravity. However, starting at about 50 km wavelength, isostatic compensation reduces the power in long-wavelength free-air gravity anomalies. It is interesting to note that both power spectra run parallel at short wavelengths and, hence, have the same scaling exponent of $\sim -4.5$.

1996). Above wavelengths of around 50 km the slope of the power spectrum decreases, indicating a reduced power for long-wavelength gravity anomalies. This is probably due to the isostatic compensation of topography (Chapin 1996), but could also indicate a limited depth extent of source, as has been shown for magnetic power spectra by Maus, Gordon & Fairhead (1997).

A power spectrum similar to Fig. 7 can be found in Chapin (1996, Fig. 3) for the free-air gravity grid of South America produced at the University of Leeds. It has a slope of around 4.7 at wavelengths below 100 km. Maus & Dimri (1996) find a scaling exponent of 4.6 for the Bouguer gravity of the Paradox Basin Salt Anticline region in Utah. These values of 4.5, 4.7 and 4.6 are fairly consistent, leading us to the conclusion

that the gravity field over land has a scaling exponent of $\gamma_g^{2D} \approx 4.5$, be it free air or Bouguer.

To investigate whether the same scaling law applies to ocean gravity, we have analysed two 8 km marine gravity grids, one off the Norwegian coast and one south of Japan. With side lengths of around 320 km the grids are much smaller than the ones for land gravity. Consequently, their power spectra are less accurate. Nevertheless, they confirm a scaling exponent of around 4.5 for ocean gravity (Fig. 8). Hence, it seems that there is no fundamental difference in the smoothness of land and marine gravity fields.

From the scaling exponent of gravity one can derive the scaling exponent of the along-track geoid as follows: with a scaling exponent of gravity $\gamma_g^{2D}$, the scaling exponent of the gravity potential is $\gamma_V^{2D} = \gamma_g^{2D} + 2$ (Maus & Dimri 1994). With Brun's formula (1) the scaling exponent of the geoid is approximately equal to the 2-D scaling exponent of the gravity potential. Furthermore, using the general relationship $\gamma^{1D} = \gamma^{2D} - 1$ we get $\gamma_{geoid}^{1D} \approx \gamma_g^{2D} + 1$. Hence, in a first approximation, the spectrum of the along-track geoid in log–log scale is expected to decrease with a slope of around 5.5 towards short wavelengths. This can be utilized as additional information in the waveform retracking.

## 7 ENFORCING A REALISTIC GEOID SOLUTION

The aim of this study is to improve the accuracy of geoid solutions derived from sea-surface height measurements. These geoid solutions are contaminated by two sources of noise. Besides the error in sea-surface height due to instrument error and atmospheric effects, the deviation between sea-surface height and geoid due to ocean dynamics is also noise in the context of this study. Here, any deviation of a geoid solution from the true geoid is referred to as noise, be it due to instrument error, ocean currents or imperfect tidal models.

Fig. 5 shows the power spectrum of along-track geoid solutions for the Atlantic Ocean. At wavelengths smaller than 50 km the OPR turns white due to high-frequency noise. In contrast, the retracked geoid solution turns white only at wavelengths shorter than 30 km. The conventional way to deal with this noise is to average and filter the along-track geoid heights until they have the desired smoothness. Hence, an optimum traveltime is picked from each waveform, the traveltimes are converted to geoid heights and finally the heights are filtered. The disadvantage of this approach is that the uncertainty of each pick, which also constitutes an important source of information, is lost prior to the filtering stage. To extract maximum information from the measurements, a realistic geoid model has to be fitted directly to the waveform data. As argued above, the power spectrum of a realistic geoid decays with a slope of approximately 5.5 towards high wavenumbers in log–log scale.

To enforce a steady slope of 5.5 at short-wavelength powers, we introduce a penalty for spline solutions with high power in high-order polynomial coefficients (=short wavelengths). This penalty is added to the misfit function in order to increase the misfit for oscillating solutions. It can vary depending on sea conditions to prevent over-damping of calm sea data. We add a simple penalty to the misfit function of eq. (3), given by

$$E' = E + \text{damp} \sum_{j=0}^{n} a_j^2 j^{\alpha}, \tag{7}$$

where damp and $\alpha$ are two parameters that are chosen by trial and error to enforce the desired spectral density of the geoid. We utilized constant values of damp $= 10^{-6}$ and $\alpha = 3$. With this penalty included in the misfit function, the coefficients of the spline polynomials are optimized in two respects, simultaneously. The corresponding traveltimes have to match the observed waveforms and the spectrum of the coefficients has to decrease with a slope of 5.5 towards short wavelengths. The result of such an inversion is shown in Figs 4 and 6. The corresponding spectrum of coefficients is shown together with the spectrum of the unconstrained inversion in Fig. 9.

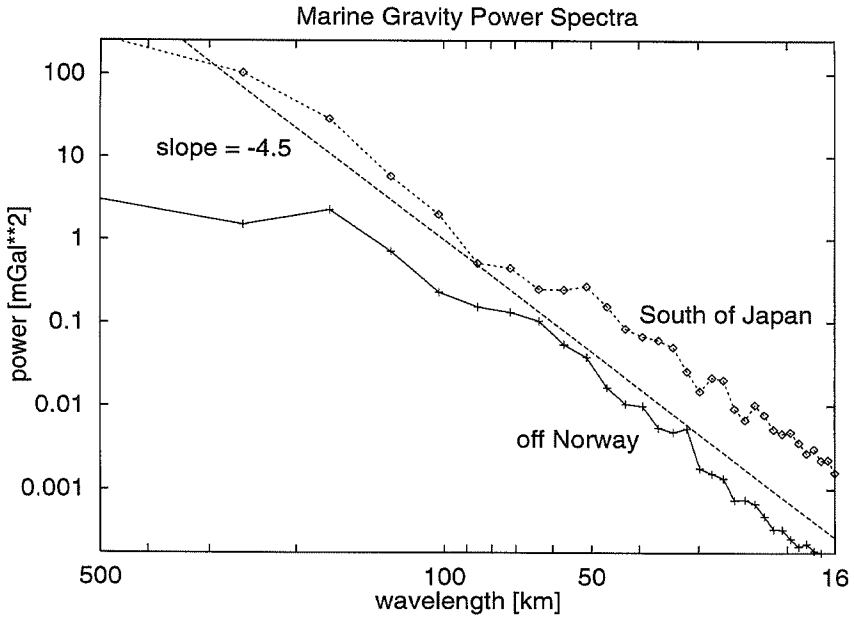


**Figure 8.** Marine gravity power spectra for 8 km grids in Lambert Conformal projection covering two areas of approximately 320 × 320 km$^2$ south of Japan and off the coast of Norway.

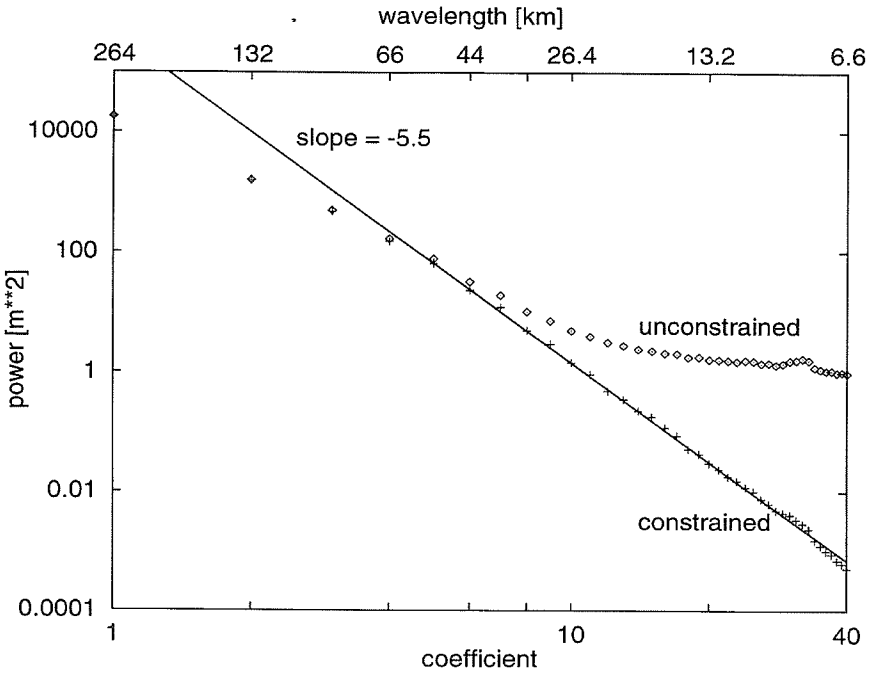


**Figure 9.** Power spectra of polynomial coefficients. The smoothness of spline geoid solutions can be controlled via the power spectrum of its polynomial coefficients. A realistic geoid power spectrum decreases with a slope of approximately −5.5 towards high coefficients.

Our approach is designed to obtain the best possible geoid solution. In a similar way one could estimate sea-surface height variations due to ocean currents. One would require a spectral model of these variations, subtract a geoid model from the sea-surface heights and invert the waveforms as described above. In this case, deviations of the geoid model from the true geoid would be considered as noise.

## 8 COHERENCE OF REPEAT TRACKS

The spatial resolution of along-track geoid solutions can be evaluated by regarding the mean squared coherence between repeat tracks (Marks & Sailor 1986; Sandwell & McAdoo 1990), defined by

$$\mathrm{coh}^2(k) = \frac{f_{\mathrm{TU}}(k)^2}{f_{\mathrm{T}}(k) f_{\mathrm{U}}(k)}, \tag{8}$$

where $k$ is the wavenumber, $f_{\mathrm{TU}}$ is the cross-spectral density and $f_{\mathrm{T}}$ and $f_{\mathrm{U}}$ are the individual spectral densities (power spectra) of tracks T and U. The coherence can be interpreted as the correlation between two signals as a function of the wavelength. If, for a given wavelength, the coherence is close to one, the information in both signals coincides and features of this wavelength are resolved. A coherence close to zero, on the other hand, indicates that the information at this wavelength is inconsistent. Coherencies of repeat track geoid solutions are close to one at long wavelengths and taper off to zero for short wavelengths. The wavelength at which the mean squared coherence falls to below 0.5 can be considered as the spatial resolution. It should be kept in mind, however, that resolution defined in this manner depends on the relative strength of signal and noise, which varies from area to area. Yale, Sandwell & Smith (1995) find an ERS-1 resolution of 50 km for a low-signal–high-noise area in the southern Pacific and 38 km for a high-signal–low-noise area at the Mid-Atlantic Ridge. For shallow areas with strong short-wavelength gravity signals, such as the continental margins, resolution may be even better.

To compare our geoid solution against the *Ocean Product* we used 42-orbit sequences of three corresponding repeat tracks from the 35-day exact repeat mission (multidisciplinary phase). We selected the Atlantic Ocean as a study area and dismissed data of latitudes greater than 60° to avoid errors due to sea ice. Waveforms over land, in ice tracking mode, or with range, waveform, tracking or location error were excluded from the analysis. Finally, we cut the along-track geoid solutions into corresponding sections in which all three repeat tracks were present, OPR as well as waveform data. From these sections (Fig. 10) the coherence between tracks was estimated using a 285 km window. The result is shown in Figs 11–13.

The overall coherence (Fig. 11) shows that the geoid solution obtained by retracking traveltimes of individual waveforms has a significantly improved resolution of 35 km over the 41 km resolution of the OPR. This resolution can be improved further to 31 km by including a geoid spectral model at the tracking stage.

To investigate the influence of the sea state on geoid resolution, we have classified all pairs of tracks into a calm group (Fig. 12), for which the mean wave height of both tracks is less than 2 m, and the complementary rough group (Fig. 13), for which at least one of the tracks has a mean wave height above 2 m. The comparison shows that while our retracked and spline geoid solutions are robust with regard to the sea state, the quality of the OPR deteriorates to 47 km at very moderate wave heights.

## 9 CONCLUSIONS

We have described a new approach towards ocean geoid estimation from satellite altimeter waveform data. Earlier

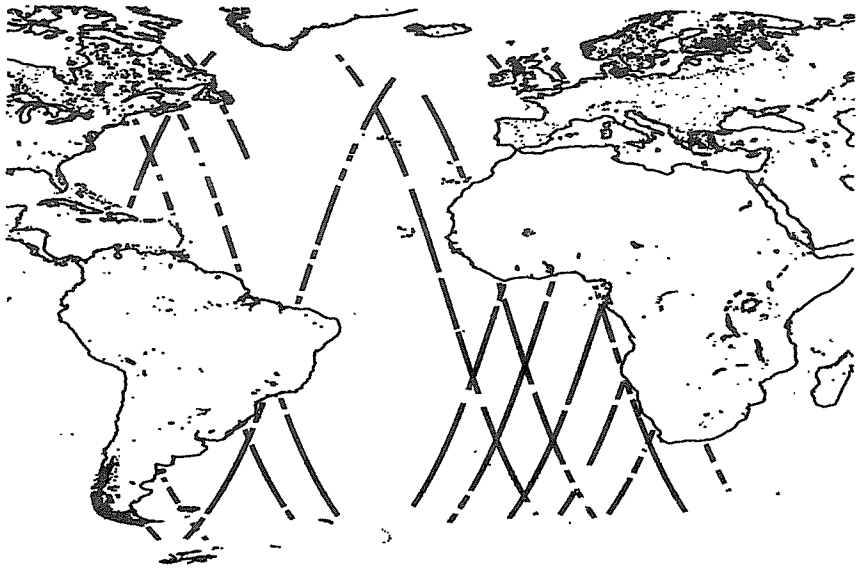

**Figure 10.** Location of sections used for estimating along-track coherence. Only tracks for which all three repeat tracks were present and free of instrument error were chosen. No data were excluded for other reasons.

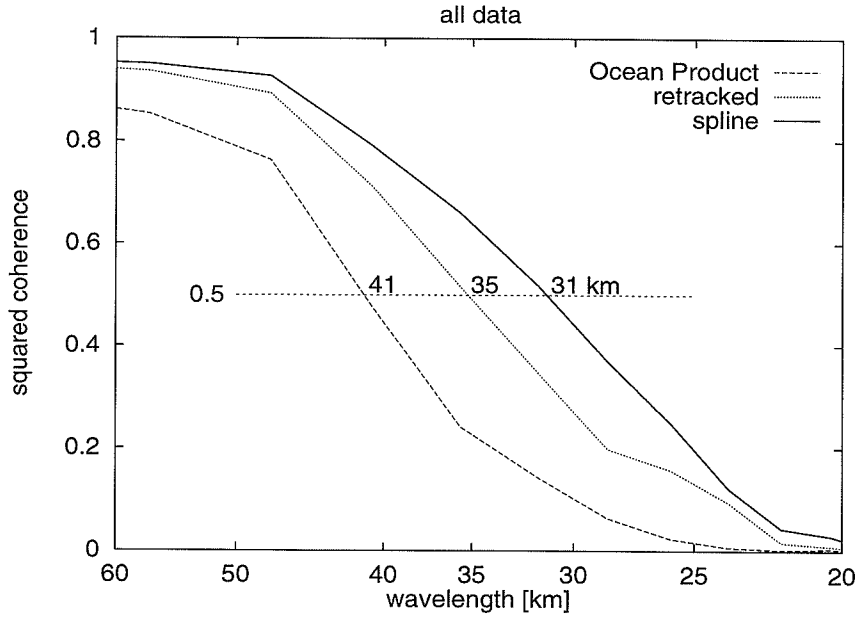


**Figure 11.** Coherence estimated from pairs of repeat tracks over the Atlantic Ocean using a 285 km window. The data are taken from three corresponding 42-orbit sequences of the 35-day multidisciplinary phase.

tracking schemes utilized complicated models attempting to explain the entire waveform. Furthermore, each waveform was inverted separately, as if it were a statistical event unrelated to the adjacent waveforms. Instead, we align a whole sequence of waveforms simultaneously. A spline geoid model is fit to the sequence of waveforms in such a way that the variance at the leading edge is minimized. By introducing a penalty for high power in high-order spline polynomial coefficients, the power spectrum of the spline solution is forced to take on the shape of the true geoid power spectrum. The coherence of repeat tracks shows a significant improvement in along-track geoid resolution from 41 to 31 km. The quality of our geoid solution is maintained at rough sea states, where an improvement from 47 to 31 km was achieved. This is particularly important for processing Geodetic Mission data where, due to the absence of repeat tracks, a noisy track cannot be substituted.

## ACKNOWLEDGMENTS

We thank Bob Janssen, Vincent Lesur, M. Anzenhofer and two anonymous reviewers for helpful comments on earlier versions of this manuscript. Stefan Maus was supported by a research fellowship NERC ROPA GR3/R9504.

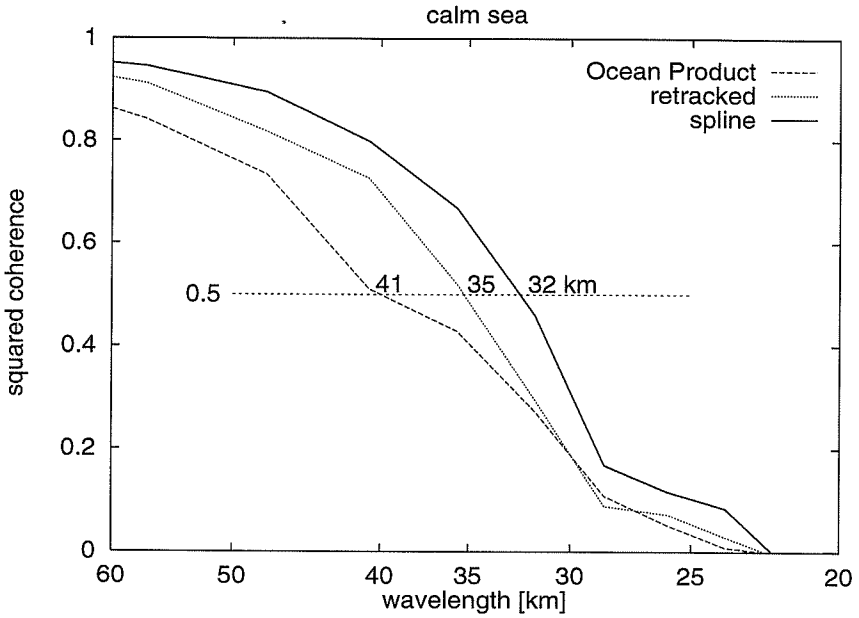


**Figure 12.** Coherence for all pairs with a mean wave height less than 2 m in both tracks.

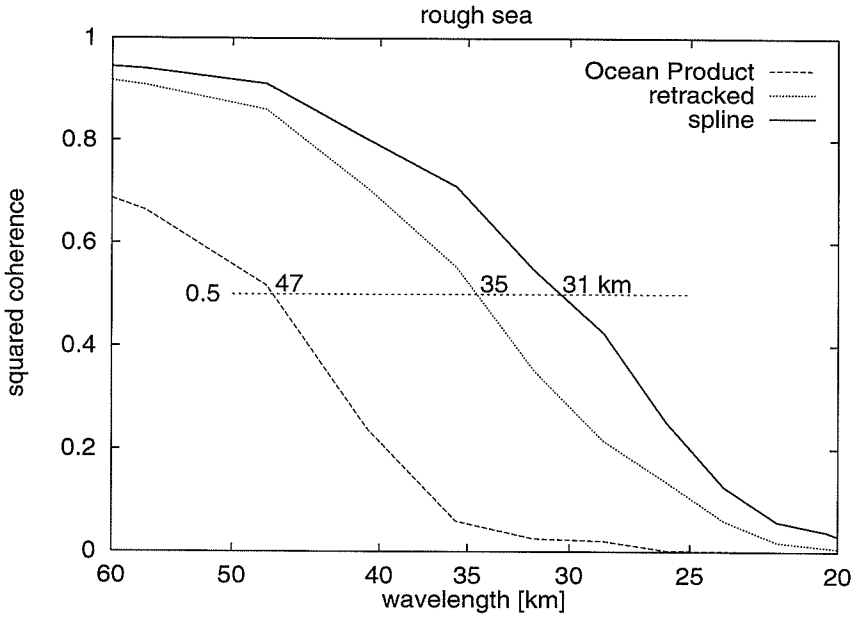


**Figure 13.** Coherence for the complementary group to Fig. 12, namely all pairs with a mean wave height of more than 2 m in at least one of the tracks. The absolute coherencies should not be compared with the absolute coherencies in Fig. 12 because they do not cover the same area. The relative difference in coherence, however, demonstrates that the quality of the OPR deteriorates significantly with increasing wave height, in contrast to this study's geoid solutions.

## REFERENCES

Brown, G.S., 1977. The average impulse response of a rough surface and its applications, *IEEE Trans. Antennas Propagat.*, **25,** 67–74.

Challenor, P.G. & Strokosz, M.A., 1989. The extraction of geophysical parameters from radar altimeter return from a non-linear sea surface, in *Mathematics in Remote Sensing,* pp. 257–268, ed. Brooks, S.R., Clarendon Press, Oxford.

Chapin, D.A., 1996. A deterministic approach towards isostatic gravity residuals—a case study from South America, *Geophysics,* **61,** 1022–1033.

Haxby, W.F., Karner, G.D., LaBreque, J.L. & Weissel, J.K., 1983. Digital images of combined oceanic and continental data sets and their use in tectonic studies, *EOS, Trans. Am. geophys. Un.,* **64,** 995–1004.

Marks, K.M. & Sailor, R.V., 1986. Comparison of GEOS-3 and SEASAT altimeter resolution capabilities, *Geophys. Res. Lett.,* **13,** 697–700.

Maus, S. & Dimri, V.P., 1994. Scaling properties of potential fields due to scaling sources, *Geophys. Res. Lett.,* **21,** 891–894.

Maus, S. & Dimri, V.P., 1996. Depth estimation from the scaling power spectrum of potential fields?, *Geophys. J. Int.,* **124,** 113–120.

Maus, S., Gordon, D. & Fairhead, J.D., 1997. Curie-temperature depth estimation using a self-similar magnetization model, *Geophys. J. Int.*, **129,** 163–168.

Olgiati, A., Balmino, G., Sarrailh, M. & Green, C.M., 1995. Gravity anomalies from satellite altimetry; comparison between computation via geoid heights and via deflections of the vertical, *Bulletin Geodesique,* **69,** 252–260.

Pilkington, M. & Todoeschuck, J.P., 1990. Stochastic inversion for scaling geology, *Geophys. J. Int.,* **102,** 205–217.

Rapp, R.H., 1983. The determination of geoid undulations and gravity anomalies from Seasat altimeter data, *J. geophys. Res.,* **88,** 1552–1562.

Sandwell, D.T. & McAdoo, D.C., 1990. high-accuracy, high-resolution gravity profiles from 2 years of Geosat exact repeat mission, *J. geophys. Res.,* **95,** 3049–3060.

Sandwell, D.T. & Smith, W.H.F., 1997. Marine gravity anomaly from Geosat and ERS-1 satellite altimetry, *J. geophys. Res.,* **102,** 10 039–10 054.

Schwarz, K.P., Sideris, M.G. & Forsberg, R., 1990. The use of FFT techniques in physical geodesy, *Geophys. J. Int.,* **100,** 485–514.

Tokmakian, R.T., Challenor, P.G., Guymer, T.H. & Srokosz, M.A., 1994. The UK EODC ERS-1 altimeter oceans processing scheme, *Int. J. Remote Sensing,* **15,** 939–962.

Yale, M.M., Sandwell, D.T. & Smith, W.H.F., 1995. Comparison of along-track resolution of stacked Geosat, ERS-1, and Topex satellite altimeters, *J. Geophys. Res.,* **100,** 15 117–15 127.